Electronic structure of amorphous indium oxide transparent conductors

J. Rosen[1] and O. Warschkow[2]
[1]*Thin Film Physics Division, Linköping University, Linköping S-581 83, Sweden*
[2]*Centre for Quantum Computer Technology, School of Physics, The University of Sydney, Sydney, New South Wales 2006, Australia*
(Received 19 May 2009; revised manuscript received 6 August 2009; published 28 September 2009)

Using empirical atomistic simulations and density functional theory (DFT), we examine the atomic and electronic structure of pure- and tin-doped indium oxide in various degrees of amorphisation. Atomic structures ranging from maximally amorphous (within fixed periodic boundary conditions) to fully crystalline are prepared using liquid-quench molecular dynamics simulations in which the cooling/quench rate is the governing parameter. The final structures are reoptimized using DFT and the electronic structure (band gaps and carrier effective masses) are compared to the crystalline material. We find that the conduction bands of In_2O_3 are quite resilient in several aspects to changes in the atomic structure. This suggests that local coordination geometries around indium and oxygen are less critical to transparent conductivity than previously thought.

DOI: 10.1103/PhysRevB.80.115215 PACS number(s): 61.43.Bn, 71.20.Nr, 71.23.Cq

I. INTRODUCTION

In_2O_3 is a transparent, wide band gap semiconductor that exhibits weak *n*-type conductivity due to the presence of intrinsic oxygen vacancies in the lattice.[1–4] Drastic increases in the carrier concentration can be achieved by doping with extrinsic *n*-type dopants, such as tin.[5–8] Interestingly, doping preserves the optical transparency of the In_2O_3 host, which gives these materials a high-application profile as transparent conductors in display technology, light emitting diodes, and other optoelectronic devices.[9] Tin-doped indium oxide (ITO) is one of the most widely used transparent conductors which has motivated numerous studies into the physical origins of combined transparency and conductivity in this material.[5,10,11] Theory and simulation have an important role in this endeavor and several works have considered crystalline In_2O_3, the electronic density of states or bandstructure,[12–21] alternative crystal structures,[19,21] intrinsic defects,[22,23] the effects of doping with Sn (Refs. 16 and 24–26) or other elements such as Mo,[17] and defect clusters.[11,25,27–29] Principally, transparent conductivity in ITO arises because the occupation of the dispersive conduction band with electrons results in a shift and widening of the energy gap; a process widely referred to as the Burstein-Moss shift.[30,31] In practice, secondary chemical mechanisms involving aptly labeled killer defects[32] limit the degree to which Sn dopant electrons become electrically activated at typical doping levels.[23,27,32] This type of theory work is clearly important to establish the baseline physics in the well-defined environment of a crystal. Many industrially grown ITO thin films however are far from perfectly crystalline: as-deposited films are generally amorphous[33–39] while an increased synthesis temperatures usually results in polycrystalline films.[36,38,40,41] This raises the important question[42] to what extent the structural and electronic properties of crystalline In_2O_3 (in pure- and Sn-doped forms) are retained in less ideally structured materials.

In order to address this question, we use atomistic liquid-quench simulations based on atomistic potentials to generate quasiamorphous structures of pure- and Sn-doped In_2O_3. These simulations effectively emulate the thermal quench processes that take place during plasma thin film deposition and produce a set of structures that range from highly amorphous to fully crystalline. We characterize these structures in terms of coordination numbers, ion pair, and angle-distribution functions. In order to gain insights into the electronic properties, we additionally perform density functional theory calculations on selected quench structures. In this we focus on the effective electron mass as one of the key criteria affecting transparent conductivity.

II. COMPUTATIONAL METHODOLOGY

Atomistic simulations of the amorphous to crystalline transition of In_2O_3 are based on the atomistic Born model of solids[43] as implemented in the General Utility Lattice Program (GULP).[44–46] The detailed algebraic form of the model used here and its parameterization for the In-Sn-O system is as described in Ref. 25. Briefly, all ions are represented as point charges interacting through Coulomb forces. In addition, Pauli-repulsion and dispersion interactions between ions are represented using pairwise Buckingham potentials. The polarization of oxygen ions is represented using the shell model.[47]

The performance of the model potential is illustrated by the data shown in Table I, comparing calculated bulk properties of bixbyite In_2O_3 and the metastable corundum polymorph with those obtained from experiment and density functional theory. The experimental lattice constants as well as the internal positions (not shown) are well reproduced, though this ought not surprise as this data formed part of the original fit set. Independent data in this table are the bulk moduli and the relative energy of the two polymorphs. These latter two quantities are somewhat larger than the density functional theory (DFT) values, but not unreasonably so. The qualitative trends, notably the lesser stability and the slightly larger bulk modulus of the corundum polymorph are well reproduced by the model potential.

Quasiamorphous structures of In_2O_3 and ITO are generated using molecular dynamics (MD) liquid-quench simulations in the canonical ensemble. As discussed in Ref. 50, the rapid liquid-quench method emulates the processes of

TABLE I. Bulk properties of In_2O_3 bixbyite and corundum polymorphs calculated using the atomistic model and density functional theory. Reported are the lattice constants, a and c, the bulk modulus B, the Murnaghan pressure derivative B', and the energy difference ΔE per formula unit between bixbyite and the metastable corundum polymorph. Bulk moduli were computed by a 9-point fit to the Murnaghan equation of state.

Polymorph	Parameter	Atomistic (this work)	GGA/US (this work)	LDA/PAW (Ref. 21)	Experiment (Refs. 48 and 49)
Bixbyite	a (Å)	10.119	10.341	10.094	10.118
	B (GPa)	222	136	174	
	B'	4.38	5.09	4.60	
Corundum	a (Å)	5.465	5.611	5.479	5.487
	c (Å)	14.667	14.778	14.415	14.510
	B (GPa)	233	140	176	
	B'	3.86	3.98	4.24	
	ΔE (eV)	0.55	0.15	0.11	

plasma deposition by assuming that an impacting ion creates a highly localized region of high temperature (i.e., a local melt also known as a thermal spike) with a cooling time sufficiently short (picoseconds) to be simulated. We limit explicit MD simulations to the molten region only; the effect of the solid material surrounding the thermal spike is represented *ad hoc* as a volume constraint such that the mass density of the simulation cell is equal to that of the surrounding solid. The thermal quench rate in the simulation is related to the ion impact energy; with more energetic ions corresponding to a larger thermal spike and in consequence a slower quench rate. As in our previous application of this method,[51] all MD runs are performed using the leapfrog Verlet algorithm and a 1-fs integration time step. The oxygen shells are assigned a shell to total mass ratio of 0.20, which results in a core-shell frequency well above (by a factor of 6) any ionic vibrational frequencies. Temperature control was achieved through velocity rescaling. The unit cell parameters are held fixed to those of relaxed crystalline In_2O_3 (a =10.119 Å)

The quench simulation itself is performed in three stages: (1) *Initial mixing*. To obtain a molten structure, a MD run of 10 ps is performed at 6000 K. (2) *Cooling*. Initial structures are taken from the equilibrated melt and are subjected to MD simulations involving a stepwise linear cooling protocol which reduces the temperature in steps of 50 K down to 300 K. A series of different quench rates is used, ranging from 2300, to 1.1 K/ps, corresponding to total quench times t_Q of between 2.5 and 5000 ps. (3) *Full relaxation*. The system at the end of the cooling simulation is fully geometry optimized at constant volume so that the energy-minimized fully quenched structure can be characterized.

The quasiamorphous and semicrystalline structures that result from these calculations are characterized using pair-distribution functions (PDF), angle-distribution functions (ADF), and ring statistics. Pair and angle-distribution functions are measures of the short-range order and are evaluated here as described in Ref. 51. For the ADF we use a In-O bond distance cutoff of 2.5 Å. We use the same cutoff for the calculation of coordination numbers around oxygen, indium, and tin atoms. The ring statistics of a bond network is a useful measure of medium-range order (see Ref. 52 and references therein). An n-fold ring is defined as a ring of n alternating In-O bonds, and the number of these rings gives insights into the connectivity of atoms beyond the nearest neighbor. In this we adopt the shortest-path (SP) convention[52] where rings containing shortcuts are not counted.

Electronic structure calculations are performed using density functional theory in the plane-wave/pseudoptential formalism as implemented in the Vienna *ab initio* simulation package (VASP).[53–56] We use the generalized-gradient approximation (PW91 functional)[57] together with ultrasoft pseudopotentials,[58,59] and a plane-wave cutoff of 300 eV. Irreducible Brillouin zone integrations for the cubic 80-atom unit cell and the 40-atom primitive cell were conducted using $2\times2\times2$ and $4\times4\times4$ Monkhorst-Pack grids,[60] respectively. A Gaussian smearing of width 0.05 eV is applied to determine the band occupations. All structures (crystalline and amorphous) are fully relaxed in the internal positions and the cell volume; however, the unit cell was constrained to maintain a cubic geometry.

III. RESULTS AND DISCUSSION

A. Liquid-quench simulations

With Fig. 1, we analyze our quench results for pure In_2O_3 in terms of the energetics of the final (quenched) structure that falls somewhere in between two well-defined energy bounds indicated by dashed horizontal lines: The lower-energy bound is the ideal crystalline limit, given by the energy of the In_2O_3 bixbyite crystal lattice. The upper energy bound is given by what we refer to as the "instant-quench" limit, which refers to structures from the melt that are directly energy minimized; thus, giving what could reasonably be considered a maximally disordered (yet locally stable) structure within the constraints of the simulation unit cell. The two horizontal lines for the instant-quench limit correspond to 80- and 320-atom cells; as discussed by us previously,[51] the energy difference between these lines indicates the degree to which the process of crystallization is

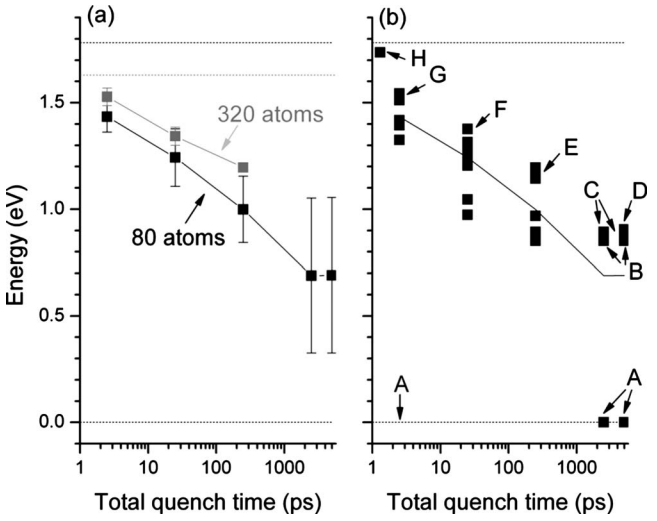

FIG. 1. Calculated energy (in eV per formula unit) of quenched In_2O_3 structures after total quench simulation times t_Q of up to 5000 ps. The upper- and lower-horizontal lines represent the energetic boundaries between an instant-quench structure (relaxation of molten arrangement) and a fully crystalline structure, respectively. (a) Average energies for 80-atom (black) and 320-atom (gray) cells. (b) Data points for all 80-atom structures. Labels indicate structures A–H which are selected for further analysis. The value quoted for 250 ps for the 320-atom cell in (a) is an average over five simulations only, as opposed to an average over 10 simulations for all others.

influenced by the use of a periodic unit cell; in the present case the effect is small.

For liquid-quench simulations carried out over finite quench times, Fig. 1(a) shows the averaged energy of the final structures as a function of quench time. The standard deviation over the results of 10 simulations is indicated by the error bars. The graph shows that the averaged energies steadily decrease with quench time, approaching, but not fully reaching the crystalline limit. The average quench time-dependent energetics of the larger 320-atom cell closely follows that of 80-atom cell up to the computationally maximum possible quench time for this cell (250 ps). For the 80-atom results at 2500 and 5000 ps the large error bars are caused by the fact that at these times two of the 10 MD simulations resulted in the crystalline bixbyite structure; thus, crystallinity is certainly emerging in our simulations.

With Fig. 1(b) we take a closer look at the individual final structures of the 10 simulations for each quench time. This reveals for the 5000 ps quench that our 10 simulations produced only four distinct structures. For the purpose of the following discussion, these four structures are labeled In_2O_3-A to In_2O_3-D (or structures A to D in short) on order of increasing energy (or decreasing stability). Of these, structure A is the ideal crystalline bixbyite structure and it was formed twice during the 5000 ps quench as mentioned above. Structure B was formed six times, and structures C and D once each. Relative to A, structures B, C, and D are 0.85, 0.89, and 0.90 eV per formula unit less stable, indicating a large energy gap between the ideally crystalline and the other three, more disordered structures. The 2500 ps simulations had a very similar outcome, with three of the same structures, namely, A, B, and C, formed two, six, and two times, respectively. Our simulations of quench times shorter than 2500 ps did not produce any crystalline bixbyite; however, several new structures result that are higher in energy than structures B, C, and D. We select three from these structures [see Fig. 1(b)] for further analysis that we label E, F, and G; one each from the 250, 25, and 2.5 ps simulation with energies of 1.18, 1.38, and 1.54 eV, respectively. Additionally, we consider as structure H a representative instant-quench (i.e., maximally disordered) structure. Together, this set of eight structure In_2O_3-A to -H covers the binding energy scale between crystalline and amorphous. Atomic views of structures A–D and H are given in Fig. 2, providing a visual sense of the increase in structural disorder.

The disorder in these structures is quantified in Fig. 3, which compares In-O pair-distribution function and the O-In-O angle-distribution function. In crystalline bixbyite In_2O_3-A [Fig. 3(a)], the In-O bond lengths to nearest neighbors range from between 2.12 and 2.21 Å, evident as sharp peaks in the pair distribution. These give rise to seven distinct peaks in the angular distribution function, the two main ones at 80° and 100°. In comparison to the crystalline structure A, the pair distribution of structures B, C, and D and H reveals an increase in the width of the first peak, and a significant broadening of the second. The increased atomic disorder is also evident from the angular distribution function, where the two most distinct peaks of structure A can still be distinguished, however with drastically reduced intensity and a large number of additional peaks. Atomic coordination numbers and shortest-path ring statistics are compared in Table II. In ideal crystalline bixbyite (i.e., structure A), all indium atoms are sixfold coordinated and all oxygen atoms are fourfold coordinated. We observe in the data that an increase in disorder over structures A–H broadly results in a

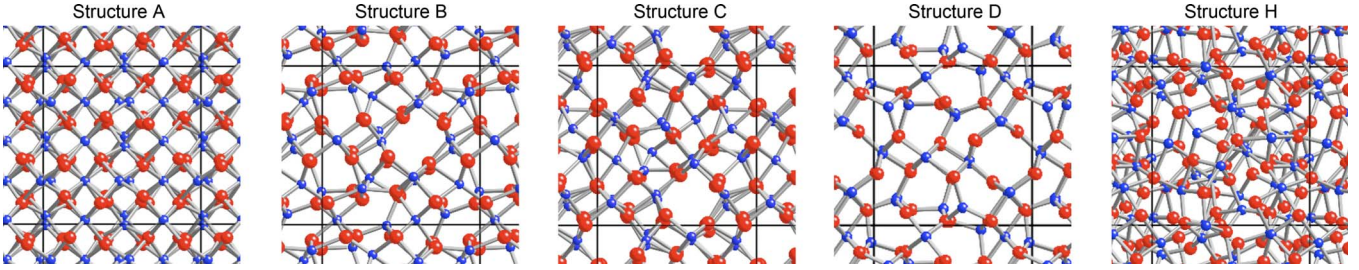

FIG. 2. (Color online) Structure views of selected final structures of In_2O_3 quench simulations ranging from fully crystalline (a) to maximally amorphous (e).

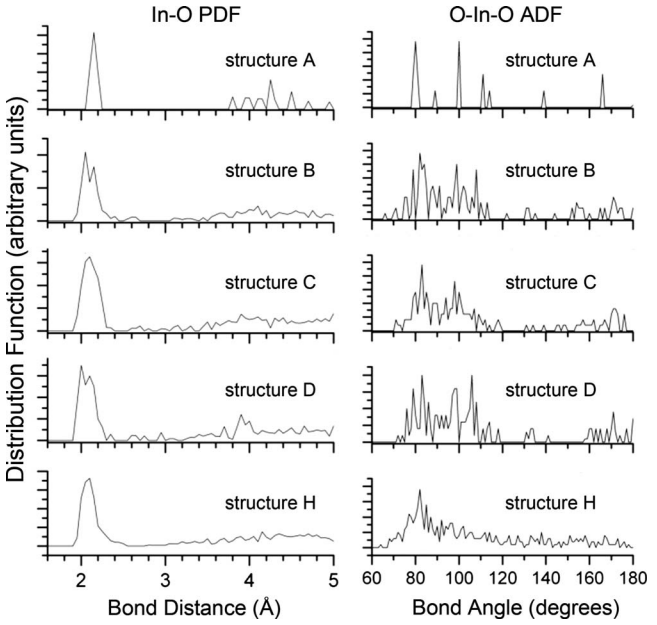

FIG. 3. Calculated In-O pair-distribution function (PDF) and O-In-O angular distribution function (ADF) for In_2O_3 structures A–D.

decrease in the average coordination number, with five- and fourfold coordinated indium and threefold coordinated oxygen sites emerging.

An analysis of medium-range order is given by the ring statistics in Table II which counts the number of shortest-path rings in the 80-atom unit cell. In crystalline In_2O_3 (structure A), four-membered rings are the most common, followed by six- and then eight-membered rings. This can be understood by reference to the fluorite lattice (CaF_2, or hypothetical "In_2O_4") from which the In_2O_3 bixbyite lattice is derived by the introduction of structural vacancies in the anion sublattice.[48] The fluorite lattice is characterized by four-membered rings only. The structural anion vacancies (two around each cation) in In_2O_3 break some of the four-membered rings, producing six- and eight-membered rings as detours through the bond network. As we go into the disordered structures in Table II, we observe a clear decrease in the number of four-membered rings and, in almost all cases, an increase in the number of six-membered rings. This can be rationalized by the reduced average coordination in the disordered structures, which leads to fewer of the four-membered rings being maintained relative to crystalline In_2O_3.

Additional liquid-quench simulations were performed for Sn-doped In_2O_3. Here, we consider both the electronically and the ionically compensated regimes that are prevalent when the material is prepared under reducing and oxidizing conditions.[5] The two regimes reflect either side of the chemical balance

$$2\mathrm{Sn}_{\mathrm{In}}^{\bullet} + 2e' + \frac{1}{2}\mathrm{O}_2 \rightleftharpoons 2\mathrm{Sn}_{\mathrm{In}}^{\bullet} + \mathrm{O}_{\mathrm{i}}'', \tag{1}$$

with the left and right hand side favored under oxygen-poor and oxygen-rich conditions, respectively. In our simulations, we replace two In^{3+} ions in the 80-atom cell by two Sn^{4+} ions, which corresponds to a Sn-doping level of 6.25 at. % and a unit cell stoichiometry of $In_{30}Sn_2O_{48}$. In the electronically compensated case, a uniform negative background charge is applied to represent the dispersed *n*-type charge carrier density and render the simulation unit cell neutral. We choose as a crystalline energy reference a structure in which the two Sn atoms substitute for indium at the Wyckoff *b* site at points of furthest separation from another. This reference structure will be labeled $[\mathrm{Sn}_{\mathrm{In}}]$-A. In the ionically compensated case, an additional oxide ion is included in the simulation cell instead of the background charge, leading to a cell stoichiometry of $In_{30}Sn_2O_{49}$. Here, the crystalline energy reference will be provided by a nearest-neighbor $2\mathrm{Sn}_{\mathrm{In}}\cdot\mathrm{O}_{\mathrm{i}}$ neutral defect cluster with both Sn atoms substituting at the Wyckoff *d* site nearest to the interstitial. This structure, labeled $[2\mathrm{Sn}_{\mathrm{In}}\cdot\mathrm{O}_{\mathrm{i}}]$-A in the following, was identified in earlier work[11,25,29] as a particularly stable defect complex.

The relative energetics of the liquid-quench simulations for the two regimes are summarized in Fig. 4. As observed for the pure In_2O_3 simulations, the averaged energies of the quenched tin-doped structures also decrease with quench time and approach the crystalline limit.

TABLE II. Coordination numbers of indium and oxygen atoms (in percent) as well as shortest-path ring statistics (number of *n*-membered rings per 80-atom unit cell) for eight selected liquid-quench structures of In_2O_3.

		Oxygen			Indium				Ring stat.		
Structure		3	4	5	4	5	6	7	4	6	8
In_2O_3	-A	0	100	0	0	0	100	0	54	30	16
	-B	38	63	0	19	19	63	0	35	46	23
	-C	38	63	0	13	31	56	0	20	44	13
	-D	58	42	0	44	0	56	0	23	46	3
	-E	42	58	0	9	44	47	0	25	42	24
	-F	46	54	0	6	56	38	0	22	35	26
	-G	58	50	2	6	59	31	3	29	27	16
	-H	33	67	0	3	44	53	0	35	38	31

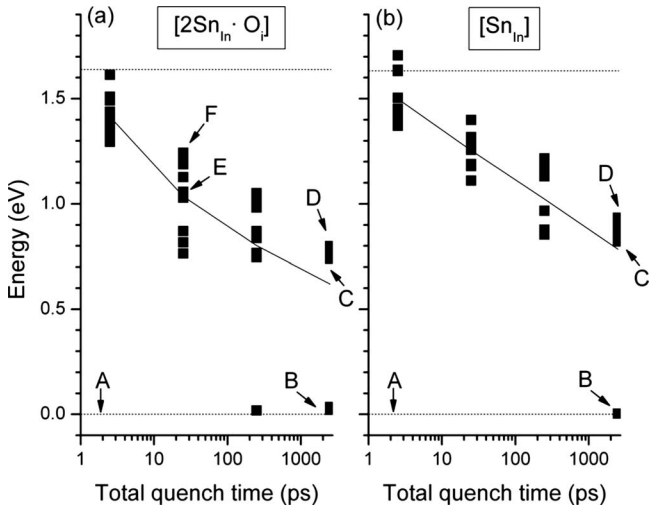

FIG. 4. Energy per formula unit of In_2O_3 relative to the initial crystalline structure, for optimized 80-atom structures for various total quench simulation times up to 2500 ps. The upper- and lower-horizontal lines represent the energetic boundaries between an instant-quench structure (relaxation of molten arrangement) and a fully crystalline structure, respectively. (a) The ionically compensated $[2Sn_{In}\cdot O_i]$ system. (b) The electronically compensated $[2Sn_{In}]$ system.

For the ionically compensated case [Fig. 4(a)], two out of the 10 simulations quenched over 2500 ps produced structures that are within 0.04 eV above the reference crystalline arrangement. Of these two, the lowest-energy structure is labeled $[2Sn_{In}\cdot O_i]$-B, and we will further analyze this structure below. The other eight simulations produced structures that are within a narrow energy interval between 0.74 and 0.80 eV. Of these, we select the lowest- and highest-energy structure as structures $[2Sn_{In}\cdot O_i]$-C and -D for further analysis. To provide insights into the effect of increased structural disorder, we additionally select two structures from the set of 25 ps simulations. Labeled structures $[2Sn_{In}\cdot O_i]$-E and -F, their energies are 1.03 and 1.24 eV above the reference crystalline arrangement.

The 10 simulations at 2500 ps for the electronically compensated case [Fig. 4(b)] resulted in one final structure that is energetically within 0.01 eV to the crystalline reference and nine structures that fall into an energy interval between 0.82 to 0.93 eV. The low-energy quench structure labeled $[Sn_{In}]$-B has recovered the crystalline bixbyite structure; however it is distinguished from the reference structure A by a different relative placement of the two substitutional Sn atoms in the cell. The lowest- and highest-energy structures from the 0.82 to 0.93 eV interval are included in our selection for further analysis and labeled $[Sn_{In}]$-C and -D, respectively.

Calculated coordination numbers for the selected structures of the $[2Sn_{In}]$ and $[2Sn_{In}\cdot O_i]$ sets are listed in Table III. For the set of tin-doped structures without compensating oxygen (set $[Sn_{In}]$), the lowest-energy structures A and B retain the coordination of the bixbyite lattice with indium sites sixfold and all oxygen sites fourfold coordinated. For the higher-energy structures C and D lower-coordination numbers emerge as a result of disorder. In particular, threefold coordinated oxygen and 4- and fivefold coordinated indium sites are formed. Similar trends are found for the ionically compensated set of structures (set $[2Sn_{In}\cdot O_i]$). Both structures A are B in this set are fully crystalline with an additional interstitial oxygen, which results in two sevenfold indium and two threefold oxygen sites apart for the regular sixfold cation and fourfold sites. Structure A is the crystalline reference with the two Sn atoms nearest to the interstitial. Structure B has a different (non-nearest) placement of Sn atoms around the interstitial. The remaining four structures C, D, E, and F are disordered as evident in the appearance of numerous sites with reduced coordination.

B. Electronic structure

The three sets of quenched structures for pure and tin-doped In_2O_3 form the basic structure input for our DFT calculations. To this end, we first reoptimize the atomistic structures using DFT so that all become local minima within DFT. Internal atomic positions as well as cubic lattice constant

TABLE III. Coordination numbers (in percent of total) of indium, oxygen, and tin atoms for selected quench structures of tin-doped In_2O_3.

		Oxygen		Indium				Tin	
Structure		3	4	4	5	6	7	5	6
$[2Sn_{In}\cdot O_i]$	-A	4	96	0	0	93	7	0	100
	-B	4	96	0	0	93	7	0	100
	-C	47	53	3	57	37	3	50	50
	-D	47	53	10	47	40	3	0	100
	-E	49	51	7	50	43	0	50	50
	-F	37	63	3	43	50	3	0	100
$[Sn_{In}]$	-A	0	100	0	0	100	0	0	100
	-B	0	100	0	0	100	0	0	100
	-C	38	63	20	20	60	0	0	100
	-D	40	60	23	13	63	0	50	50

TABLE IV. Calculated formation energies of selected pure and Sn-doped In_2O_3 quench structures (see text) as a function of total quench time t_Q. All structures were further relaxed using DFT and the obtained energies and optimized cubic lattice constants a are also reported. All energies are given per formula unit In_2O_3 relative to the reference crystalline structure.

Structure		Quench time t_Q (ps)	Atomistic E (eV)	DFT E (eV)	DFT a (Å)
In_2O_3	-A	reference	0.00	0.00	10.34
	-B	5000	0.85	0.48	10.45
	-C	5000	0.89	0.49	10.43
	-D	5000	0.90	0.50	10.52
	-E	250	1.18	0.68	10.52
	-F	25	1.38	0.79	10.50
	-G	2.5	1.54	0.89	10.58
	-H	instant	1.74	0.99	10.53
$[2Sn_{In} \cdot O_i]$	-A	reference	0.00	0.00	10.37
	-B	2500	0.02	0.01	10.37
	-C	2500	0.74	0.44	10.47
	-D	2500	0.80	0.45	10.50
	-E	25	1.03	0.63	10.51
	-F	25	1.24	0.70	10.41
$[Sn_{In}]$	-A	reference	0.00	0.00	10.38
	-B	2500	0.00	0.00	10.38
	-C	2500	0.82	0.43	10.46
	-D	2500	0.93	0.49	10.47

were optimized; the cell shape however was constrained to remain cubic. Overall, we found that these optimizations led only to small adjustments in bond distances and angles; that is, the structures as obtained by the atomistic quench model are qualitatively preserved in DFT.

Table IV summarizes the structure and energy results of these calculations. We find that atomistic and DFT formation energies are well correlated; however, the DFT energies are consistently smaller (about 50%–60% of the atomistic value). Important for the validity of the atomistic model in regard to the quench simulations is that both models agree on the energetic order of all the structures in every set. Looking now at the relaxed cubic lattice constant a, we generally find a small increase of up to 2% in the disordered structures relative to crystalline In_2O_3 and the reference structures of each set. A clear correlation between relative energy (as a measure of disorder) and the lattice constant however is not apparent.

Before considering the electronic structure of disordered indium oxide and indium-tin-oxide, we briefly discuss, for reference, the band structure of crystalline In_2O_3 and 6.25 at. % Sn-doped In_2O_3. Figure 5 shows for these two systems the electronic band structure along the high-symmetry directions of the 40-atom primitive cell of bixbyite. Our band structure results are in good qualitative agreement with those previously reported[14–21,24] with near-flat bands at the valence band maximum, and the lowest-conduction band highly dispersed. For undoped crystalline In_2O_3, our calculated band gap E_g^Γ is 0.79 eV. This is slightly smaller than previously reported DFT values of 0.93,[18] 1.10,[19] 1.12,[21] and about 1 eV,[16] but within the range of variation due to choice of DFT functional and

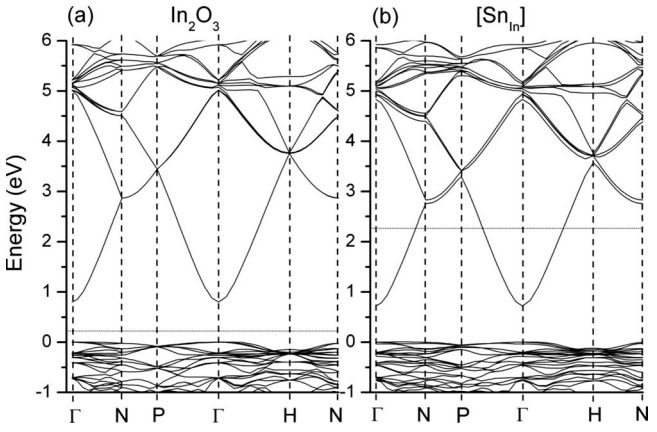

FIG. 5. The calculated band structure for 40-atom primitive unit cells of (a) crystalline bixbyite In_2O_3 and (b) Sn-doped In_2O_3 with Sn substituting at the Wyckoff b site. Band energies are referenced to the top of the valence band. The Fermi levels at 0.22 and 2.27 eV, respectively, are indicated by a horizontal dotted line.

pseudopotential.[62] Band gaps calculated by DFT are generally smaller than the corresponding experimental values. For In_2O_3 there exists considerable ambiguity over the nature and value of the experimental band gap. Widely quoted is an experimental band gap of 3.75 eV;[61] however, weaker transitions occur at energies as low as 2.6 eV, which have been attributed to an indirect band gap.[61] A recent study[20] revises this interpretation, concluding that the experimental gap is smaller than 2.9 eV, although optical transitions are dipole weak when bands up to 0.8 eV below the valence band minimum are involved.

In our discussion, we will focus on a quantity of particular relevance to the conductivity of a material, namely, the effective mass m^* of the n-type charge carriers in the lowest highly dispersive conduction band. We calculate the effective mass numerically via the curvature $\partial^2 E(k)/\partial k^2$ of the lowest-conduction band at the Γ point. Band energies for small displacements in k covering less than 1/10 of the Γ-H, -N, and -P distances are fitted to the equation

$$E(k) = E_g^{\Gamma} + \frac{\hbar^2 k^2}{2m^*}, \tag{2}$$

in which E_g^{Γ} is the energy gap at the Γ point and band energies are given relative to the valence band maximum at the Γ point. Using this procedure, we obtain effective masses m^* of 0.16, 0.15, and 0.15 electron masses (m_e) for the Γ-H, -N, and -P directions, respectively. There is a point of technical subtlety here that must be kept in mind when comparing our results to those reported by others.[14,19,26] Away from the Γ point and toward the zone boundaries, the lowest-conduction band becomes increasingly nonparabolic and exhibits an almost linear $E(k)$ dependence [see Fig. 5(a)]. As a consequence, fitting of Eq. (2) over a larger range of k space would result in larger effective masses. For instance, Eq. (2) fitted over the full Γ-H, -N, and -P distance produces effective masses of 0.48, 0.34, and 0.40 m_e, respectively. It appears, this latter procedure was adopted in Refs. 14 and 26 which report masses in the range of 0.30 to 0.42 and 0.31 to 0.54 m_e, respectively. In contrast, Karazhanov *et al.*[19] perform a high-order polynomial fit and report masses between 0.20 and 0.23 m_e; these values are more in line with our near-Γ results of 0.15 to 0.16 m_e. The experimental effective mass of conduction band electrons in In_2O_3 is reported to be approximately 0.3 m_e.[63–65] From the above discussion, this suggest some degree of mass averaging over the Brillouin zone in the measurement. We note in passing, that our choice of pseudopotential (ultrasoft vs projector-augmented wave) and exchange-correlation functional (PW91 vs LDA) had a comparatively minor effect on the calculated effective masses.

For our discussion of quasiamorphous structures in 80-atom periodic unit cells we consider effective masses that are averaged over directions. These averages we calculate numerically using small displacements from Γ along the six ⟨001⟩(Γ-X), twelve ⟨011⟩(Γ-M), and eight ⟨111⟩(Γ-R) directions and fitting to Eq. (2). The directionally averaged effective mass for crystalline In_2O_3 evaluates to 0.15 m_e.

Table V summarizes our results for the series of undoped

TABLE V. Electronic structure analysis of quenched In_2O_3 structures. We report the fundamental band gaps E_g^{Γ}, the Fermi-level E_F relative to the top of the valence band, and average effective electron mass m^* of the lowest-conduction band.

Structure		E_g^{Γ} (eV)	E_F (eV)	m^* (m_e)
In_2O_3	-A	0.79	0.29	0.15
	-B	0.71	0.28	0.16
	-C	0.64	0.23	0.16
	-D	0.74	0.28	0.15
	-E	0.47	0.28	0.15
	-F	0.33	0.28	0.15
	-G	0.32	0.17	0.15
	-H	0.02	0.28	0.11

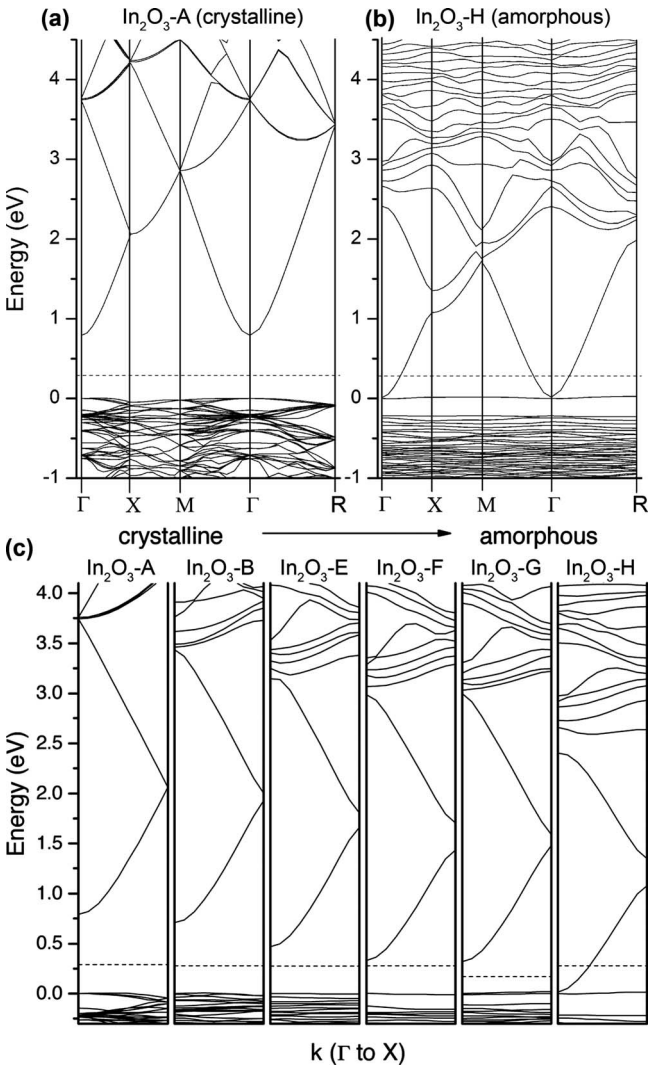

FIG. 6. Calculated band structure in a cubic 80-atom unit cell of (a) crystalline In_2O_3 (structure A) and (b) maximally amorphous In_2O_3 (structure H). Shown below (c) is a comparison of band structure along one segment (Γ-X) for six structures of the In_2O_3 quench series.

TABLE VI. Electronic structure parameter of quenched In_2O_3 structures containing 6.25 at. % substitutional Sn (set $[Sn_{In}]$). We report the Fermi-level E_F relative to the valence band maximum as well as the effective electron mass m^* of the lowest-conduction band. Also given for reference are the values for the undoped crystalline In_2O_3 (structure In_2O_3-A; cf. Table V).

	$[Sn_{In}]$-A	$[Sn_{In}]$-B	$[Sn_{In}]$-C	$[Sn_{In}]$-D	In_2O_3-A
E_g^Γ (eV)	0.68	0.62	0.57	0.58	0.79
E_F (eV)	2.06	1.99	1.83	1.94	0.29
m^* (m_e)	0.14	0.14	0.15	0.15	0.15

In_2O_3 structures A to H, reporting the fundamental band gap (E_g^Γ), the Fermi level (E_F), and the average effective mass (m^*). Figure 6 shows the full band structure for a cubic 80-atom cell of crystalline and maximally amorphous In_2O_3 as well as a segment of the band structure for six of the quenched structures. Going from the ideally crystalline structure A to the maximally disordered structure H, we observe in the data a broadly decreasing trend in the calculated band gap. Inspection of the band structure of the maximally amorphous In_2O_3-H [Fig. 6(b)] shows that much of the qualitative structure of the crystalline conduction band [In_2O_3-A, Fig. 6(a)] is preserved, albeit shifted to lower-energy relative to the valence band. Figure 6(c) illustrates how the conduction bands and the valence bands approach each other across the set of quenched In_2O_3 structures which further highlights the similarities in the dispersive characteristics of the lowest-conduction band. This is also evident in the calculated effective masses (Table V) which show hardly any changes across the set. At the X zone boundary in Fig. 6(c), a gap opens in the conduction band for all but the ideally crystalline structure, reflecting the increased probability for carrier scattering with loss of crystalline order.

In the amorphous structure H [see Figs. 6(b) and 6(c)], the dispersed conduction band and the highest valence band touch, resulting in an electronic structure that is metallic and has some occupation of the conduction band. The highest valence band is a single flat band that is well separated from the other valence states. From the electronic structure alone it may be tempting to label this band a defect level in the gap, however, a defect is not easily defined in a structure as disordered as structure H. The electron density associated with this band is of $2p$ character and highly localized on two oxygen atoms. One of the oxygen atoms is threefold coordinated, the other is a fourfold site, and the two atoms share one indium atoms in their coordination spheres. These features of the coordination environment are not unusual. There are two aspects that could be causative to the upshift in this band: the separation between the two oxygen atoms is relatively small (2.52 Å), the band density is localized and $2p$ shaped on these atoms, and directed toward each other. Close proximity plausibly leads to an increased repulsion between these sites, which brings this band close to the conduction band, which in turn results in a degree of thermal cross population. Note though, that cause and effect could be argued in reverse in that it is the partial depopulation of these two O-$2p$ levels by the conduction band, which pulls these atoms toward each other. Either way, disorder has produced in this structure a degree of intrinsic population of the dispersed conduction band. We will encounter these upshifted valence levels again in our later discussion on doped In_2O_3.

The changes in band structure evolution with disorder for the set of Sn-doped structures without interstitial oxygen (i.e., structures $[Sn_{In}]$-A to -D) is very similar to that of clean In_2O_3. The data in Table VI reveals a small reduction in fundamental band gap for the disordered structures and little change in the calculated effective masses, both within the set and relative to undoped In_2O_3. As in the crystalline Sn-doped case [cf. Figure 5(b)], the quenched structures have the Fermi level raised high into the conduction band due to the extra n-type charge carriers. The overall morphology of crystalline conduction band structure is well-preserved into the disordered structures.

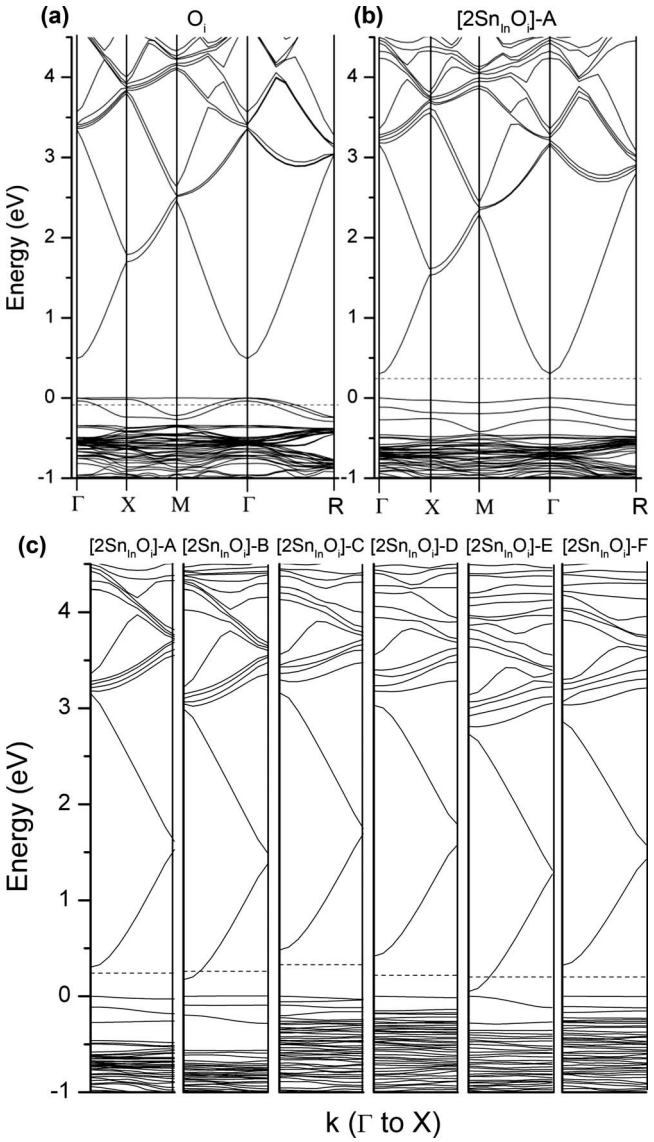

FIG. 7. Calculated band structure of (a) interstitial oxygen O_i'', and (b) a nearest-neighbor $[2Sn_{In} \cdot O_i]$ defect cluster in a 80-atom cubic unit cell of crystalline In_2O_3. (c) Partial band structure along Γ to X for the five $[2Sn_{In} \cdot O_i]$ quench structures A–E.

TABLE VII. Electronic structure parameter of the $[2Sn_{In}\cdot O_i]$ set of quenched structures.

	$[2Sn_{In}\cdot O_i]$-A	-B	-C	-D	-E	-F
E_g^{Γ} (eV)	0.30	0.17*	0.48	0.42	0.05*	0.32
E_F (eV)	0.24	0.26	0.32	0.22	0.20	0.20
m^* (m_e)	0.15	0.15	0.15	0.13	0.16	0.15

The electronic structure of the $[2Sn_{In}\cdot O_i]$ set of ionically compensated structures of tin-doped In_2O_3 exhibits a somewhat more irregular behavior. In order to describe this it is worthwhile to examine first the band structures of crystalline In_2O_3 containing [Fig. 7(a)] a single interstitial oxygen atom (O_i'') and [Fig. 7(b)] a $2Sn_{In}\cdot O_i$ nearest-neighbor defect cluster. In the cluster both Sn atoms are located at Wyckoff *d* sites nearest to the interstitial (see Ref. 29). The full electronic band structure of the interstitial is shown in Fig. 7(a) and it is characterized by three weakly dispersed bands that are offset above the remainder of the valence bands (see also Ref. 17). These bands are primarily due to the O-2*p* levels of the interstitial, which appear as defect levels in the gap above the valence band. The Fermi-level cuts through these levels, because the doubly negatively charged interstitial (O_i'') is electronically compensated by two electron holes ($2\ h^{\bullet}$). In the defect cluster [Fig. 7(b)], the same interstitial bands appear, but these are now below the Fermi level. Here, the Sn atoms provide the compensation for the oxygen interstitial, however, this consumes the two Sn donor electrons and makes them unavailable as carriers for the conduction band. While the Fermi level is raised above the interstitial bands, it remains below the conduction band minimum. This behavior is well-understood; the deactivation of Sn donors by clustering with interstitial oxygen is the basis of long-standing models[5] describing the observed dependence of ITO charge carrier densities on O_2 exposure during sample preparation/anneal.

In the quenched $[2Sn_{In}\cdot O_i]$ structures [Fig. 7(c)], owing to the increased disorder, the compensation of interstitial valence defect levels by Sn dopants is less effective. Three of the five quenched structure (namely, $[2Sn_{In}\cdot O_i]$-C, -D, and -F) exhibit a qualitatively similar band structure to the crystalline defect (structure A). Several of the valence bands are slightly upshifted toward the conduction band, which leads to a smaller fundamental band gap (see Table VII). In these structures, the Fermi level is below the conduction band which means that ionic compensation between Sn dopants and the excess oxygen atom is effective. For the other two structures ($[2Sn_{In}\cdot O_i]$-B and -E) however isolated valence bands (and the Fermi level) are shifted above the conduction band minimum, resulting in an electronic structure that is metallic with some population of the lowest-conduction band. As in case of the undoped, amorphous In_2O_3 structure H, these upshifted bands are of O-2*p* character involving pairs of oxygen atoms in close proximity. So we can understand these disordered structures to have oxygen atoms in positions that compromise their ability to act as electron acceptors. In consequence, the ionic compensation mechanism by which the Sn donor electrons are trapped on the excess oxygen atom is rendered ineffective.

IV. SUMMARY AND CONCLUSIONS

In summary, we have modeled the structural and electronic properties of In_2O_3 and ITO of varying degree of structural disorder using a combination of atomistic and DFT methods. We find that the overall morphology of the conduction band structure of crystalline In_2O_3 is largely maintained even in highly disorder structures. Calculated average effective masses for the lowest-conduction band exhibit only minor changes of below 5%. These findings correlate well with earlier experimental studies[33] into the electron transport properties of amorphous In_2O_3 films that point to a weak scattering effect of structural disorder. Our results also support recent ideas[41,42] that the pronounced metal *s*-band character of the conduction band causes typical transparent oxide semiconductors (ZnO, In_2O_3, and SnO_2) to be more resilient to bond-angular disorder than semiconductors with a more *p*-like conduction band (e.g., silicon). In our calculations, the largest effect of disorder is a reduction in the fundamental band gap as valence band maximum and conduction band minimum approach each other. Disorder also results in isolated valence bands being shifted toward the conduction band (occasionally even to above the conduction band minimum), which leads in some cases to an intrinsic creation of charge carriers in the conduction band. Structural inspection suggests that these shifted bands are due to pairs of oxygen atoms which are in close proximity within the disordered structure. Our results are important to further our understanding of varying material properties of industrially grown ITO thin films, as these typically exhibit some degree of disorder, ranging from polycrystalline to fully amorphous.

ACKNOWLEDGMENTS

This work was supported by the Swedish Foundation for Strategic Research (SSF) Centre for Materials Science for Nanoscale Surface Engineering (MS^2E), the Australian Research Council, the Australian Government, the Australian Partnership for Advanced Computing, and the U.S. Advanced Research and Development Activity, National Security Agency, and Army Research Office under Contract No. DAAD19-01-1-0653.

[1] G. Rupprecht, Z. Phys. **139**, 504 (1954).
[2] R. L. Weiher, J. Appl. Phys. **33**, 2834 (1962).
[3] J. H. W. De Wit, J. Solid State Chem. **13**, 192 (1975).
[4] J. H. W. De Wit, J. Phys. Chem. Solids **38**, 819 (1977).
[5] G. Frank and H. Köstlin, Appl. Phys. A: Mater. Sci. Process. **27**, 197 (1982).
[6] I. Hamberg and C. Granqvist, J. Appl. Phys. **60**, R123 (1986).
[7] C. G. Granqvist and A. Hultåker, Thin Solid Films **411**, 1

(2002).
[8] L. Bizo, J. Choisnet, and B. Raveau, Mater. Res. Bull. **41**, 2232 (2006).
[9] D. S. Ginley and C. Bright, MRS Bull. **25**, 15 (2000).
[10] J. C. C. Fan and J. B. Goodenough, J. Appl. Phys. **48**, 3524 (1977).
[11] G. B. González, T. O. Mason, J. P. Quintana, O. Warschkow, D. E. Ellis, and J.-H. Hwang, J. Appl. Phys. **96**, 3912 (2004).
[12] E. A. Albanesi, S. J. Sferco, I. Lefebvre, G. Allan, and M. Lannoo, Solid State Commun. **86**, 27 (1993).
[13] I. Tanaka, M. Mizuno, and H. Adachi, Phys. Rev. B **56**, 3536 (1997).
[14] H. Odaka, S. Iwata, N. Taga, S. Ohnishi, Y. Kaneta, and Y. Shigesato, Jpn. J. Appl. Phys. **36**, 5551 (1997).
[15] Y. Mi, H. Odaka, and S. Iwata, Jpn. J. Appl. Phys. **38**, 3453 (1999).
[16] O. N. Mryasov and A. J. Freeman, Phys. Rev. B **64**, 233111 (2001).
[17] J. E. Medvedeva, Phys. Rev. Lett. **97**, 086401 (2006).
[18] P. Erhart, A. Klein, R. G. Egdell, and K. Albe, Phys. Rev. B **75**, 153205 (2007).
[19] S. Zh. Karazhanov, P. Ravindran, P. Vajeeston, A. Ulyashin, T. G. Finstad, and H. Fjellvåg, Phys. Rev. B **76**, 075129 (2007).
[20] A. Walsh, J. L. F. DaSilva, S.-H. Wei, C. Körber, A. Klein, L. F. J. Piper, A. DeMasi, K. E. Smith, G. Panaccione, P. Torelli, D. J. Payne, A. Bourlange, and R. G. Egdell, Phys. Rev. Lett. **100**, 167402 (2008).
[21] F. Fuchs and F. Bechstedt, Phys. Rev. B **77**, 155107 (2008).
[22] T. Tomita, K. Yamashita, Y. Hayafuji, and H. Adachi, Appl. Phys. Lett. **87**, 051911 (2005).
[23] S. Lany and A. Zunger, Phys. Rev. Lett. **98**, 045501 (2007).
[24] H. Odaka, Y. Shigesato, T. Murakami, and S. Iwata, Jpn. J. Appl. Phys. **40**, 3231 (2001).
[25] O. Warschkow, D. E. Ellis, G. B. González, and T. O. Mason, J. Am. Ceram. Soc. **86**, 1700 (2003).
[26] S. H. Brewer and S. Franzen, Chem. Phys. **300**, 285 (2004).
[27] O. Warschkow, D. E. Ellis, G. B. González, and T. O. Mason, J. Am. Ceram. Soc. **86**, 1707 (2003).
[28] T. M. Inerbaev, R. Sahara, H. Mizuseki, Y. Kawazoe, and T. Nakamura, Mater. Trans. **48**, 666 (2007).
[29] O. Warschkow, Lj. Miljacic, D. E. Ellis, G. B. González, and T. O. Mason, J. Am. Ceram. Soc. **89**, 616 (2006).
[30] E. Burstein, Phys. Rev. **93**, 632 (1954).
[31] T. S. Moss, Proc. Phys. Soc. London, Sect. B **67**, 775 (1954).
[32] A. Zunger, Appl. Phys. Lett. **83**, 57 (2003).
[33] J. R. Bellingham, W. A. Phillips, and C. J. Adkins, J. Phys.: Condens. Matter **2**, 6207 (1990).
[34] B. Pashmakov, B. Claflin, and H. Fritzsche, Solid State Commun. **86**, 619 (1993).
[35] P. K. Song, H. Akao, M. Kamei, Y. Shigesato, and I. Yasui, Jpn. J. Appl. Phys. **38**, 5224 (1999).
[36] B. Radha Krishna, T. K. Subramanyam, B. Srinivasulu Naidu, and S. Uthanna, Opt. Mater. **15**, 217 (2000).
[37] H. J. Kim, J. W. Bae, J. S. Kim, K. S. Kim, Y. C. Jang, G. Y. Yeom, and N.-E. Lee, Surf. Coat. Technol. **131**, 201 (2000).
[38] H. Nakazawa, Y. Ito, E. Matsumoto, K. Adachi, N. Aoki, and Y. Ochiai, J. Appl. Phys. **100**, 093706 (2006).
[39] F. Utsuno, H. Inoue, I. Yasui, Y. Shimane, S. Tomai, S. Matsuzaki, K. Inoue, I. Hirosawa, M. Sato, and T. Honma, Thin Solid Films **496**, 95 (2006).
[40] C.-H. Yang, S.-C. Lee, S.-C. Chen, and T.-C. Lin, Mater. Sci. Eng., B **129**, 154 (2006).
[41] H. Hosono, J. Non-Cryst. Solids **352**, 851 (2006).
[42] J. Robertson, Phys. Status Solidi B **245**, 1026 (2008).
[43] M. Born and K. Huang, *Dynamical Theory of Crystal Lattices* (Oxford University Press, Oxford, 1954).
[44] J. D. Gale, J. Chem. Soc., Faraday Trans. **93**, 629 (1997).
[45] J. D. Gale and A. L. Rohl, Mol. Simul. **29**, 291 (2003).
[46] J. D. Gale, Z. Kristallogr. **220**, 552 (2005).
[47] B. G. Dick, Jr. and A. W. Overhauser, Phys. Rev. **112**, 90 (1958).
[48] M. Marezio, Acta Crystallogr. **20**, 723 (1966).
[49] R. D. Shannon, Solid State Commun. **4**, 629 (1966).
[50] N. A. Marks, Phys. Rev. B **56**, 2441 (1997).
[51] J. Rosen, O. Warschkow, D. R. McKenzie, and M. M. M. Bilek, J. Chem. Phys. **126**, 204709 (2007).
[52] D. S. Franzblau, Phys. Rev. B **44**, 4925 (1991).
[53] G. Kresse and J. Hafner, Phys. Rev. B **47**, 558 (1993).
[54] G. Kresse and J. Hafner, Phys. Rev. B **49**, 14251 (1994).
[55] G. Kresse and J. Furthmüller, Comput. Mater. Sci. **6**, 15 (1996).
[56] G. Kresse and J. Furthmüller, Phys. Rev. B **54**, 11169 (1996).
[57] J. P. Perdew, J. A. Chevary, S. H. Vosko, K. A. Jackson, M. R. Pederson, D. J. Singh, and C. Fiolhais, Phys. Rev. B **46**, 6671 (1992).
[58] D. Vanderbilt, Phys. Rev. B **41**, 7892 (1990).
[59] G. Kresse and J. Hafner, J. Phys.: Condens. Matter **6**, 8245 (1994).
[60] H. J. Monkhorst and J. D. Pack, Phys. Rev. B **13**, 5188 (1976).
[61] R. L. Weiher and R. P. Ley, J. Appl. Phys. **37**, 299 (1966).
[62] Using projector-augmented wave (PAW) core potentials instead of ultrasoft pseudopotentials together with a larger plane-wave cutoff of 400 eV results in a calculated direct band gap of 0.95 eV. By using the local density approximation (LDA) with PAW potentials instead of the GGA functional, the band gap is further raised to 1.17 eV in good agreement with the results of Refs. 19 and 21 (1.10 and 1.12 eV, respectively). All band gaps were calculated for a unit cell that is fully relaxed at the respective level of theory.
[63] Y. Ohhata, F. Shinoki, and S. Yoshida, Thin Solid Films **59**, 255 (1979).
[64] M. Jarzebski, Phys. Status Solidi A **71**, 13 (1982).
[65] I. Hamberg, C. G. Granqvist, K. F. Berggren, B. E. Sernelius, and L. Engström, Phys. Rev. B **30**, 3240 (1984).